Robustness of s-Wave Pairing in Electron-Overdoped $A_{1-y}Fe_{2-x}Se_2$ (A = K,Cs)

Chen Fang,[1] Yang-Le Wu,[2] Ronny Thomale,[2] B. Andrei Bernevig,[2] and Jiangping Hu[1,3]

[1]*Department of Physics, Purdue University, West Lafayette, Indiana 47907, USA*
[2]*Department of Physics, Princeton University, Princeton, New Jersey 08544, USA*
[3]*Beijing National Laboratory for Condensed Matter Physics, Institute of Physics, Chinese Academy of Sciences, Beijing 100080, China*

(Received 5 May 2011; published 15 September 2011)

Using self-consistent mean-field and functional renormalization-group approaches, we show that s-wave pairing symmetry is robust in the heavily electron-doped iron chalcogenides $AFe_{2-x}Se_2$, where A = K,Cs. Recent neutron scattering experiments suggest that the effective nearest-neighbor spin exchange may be ferromagnetic in chalcogenides. This is different from the iron pnictides, where the nearest-neighbor magnetic exchange coupling is believed to be antiferromagnetic and leads to strong competition between s-wave and d-wave pairing in the electron-overdoped region. Our finding of a robust s-wave pairing in (K,Cs)$Fe_{2-x}Se_2$ differs from the d-wave pairing result obtained by other theories where nonlocal bare interaction terms and the next-to-nearest-neighbor J_2 term are underestimated. Detecting the pairing symmetry in (K,Cs)$Fe_{2-x}Se_2$ may hence provide important insights regarding the mechanism of superconducting pairing in iron-based superconductors.

DOI: 10.1103/PhysRevX.1.011009 Subject Areas: Condensed Matter Physics, Strongly Correlated Materials, Superconductivity

I. INTRODUCTION

The recent discovery of a new family of iron-based superconductors A(K,Cs,Rb)$_y$$Fe_{2-x}Se_2$ [1–3] has initiated a new round of research in this field. Remarkably, this new family shows distinctly different properties from other pnictide families: the compounds are heavily electron-doped, but their superconducting transition temperatures are high, at more than 40 K. For comparison, such large transition temperatures (T_c's) can be reached only in the optimally doped 122 iron pnictides [4]. (''122 iron pnictides'' are those with the generic stoichiometric formula AFe_2As_2.) Importantly, both angle-resolved photoemission spectroscopy (ARPES) [5–7] and local-density approximation calculations [8–10] show the presence of only electron Fermi pockets located at the M point of the folded Brillouin zone (BZ). (Some signature of the possible density of states at the Γ point is still under debate; in any case, this pocket, if present, is assumed to be very flat and shallow.) ARPES experiments have also reported large isotropic superconducting gaps at these pockets [5–7]. The absence of hole pockets around the Γ point of the BZ provides a new arena of Fermi-surface topology in which to investigate the pairing symmetries and mechanisms of superconductivity proposed for iron-based superconductors from a variety of approaches [11–35].

So far, the majority of theories for the pairing symmetry of iron-based superconductors is based on weak-coupling approaches [13–18,27–32,36,37]. Although there are discrepancies among them, the theories based on these approaches have reached a broad consensus regarding the pairing symmetry in iron-based superconductors: For optimally hole-doped iron pnictides, for example, $Ba_{0.6}K_{0.4}Fe_2As_2$, an extended s-wave pairing symmetry, called $s^{\pm}$, is favored [14] (the sign of the order parameter changes between hole and electron pockets and is potentially detectable through neutron scattering [38]), as a result of repulsive interband interactions and nesting between the hole and electron pockets. For extremely hole-doped materials, such as KFe_2As_2, the absence of electron pockets can lead to a d-wave pairing symmetry [18] with a low transition temperature. For electron-doped materials such as $Ba_2Fe_{2-x}Co_xAs_2$, the anisotropy of the superconducting gap around the electron pockets in the $s^{\pm}$ state grows for larger electron doping, and eventually the superconducting gap develops nodes around the electron pockets due to the weakening of the nesting condition and the increase of the d_{xy} orbital weight at the electron pocket Fermi surfaces [39,40]. Finally, in the limit of the heavily electron-doped case when the hole pockets vanish and only the electron pockets are left, the d-wave pairing symmetry may be favored again [18,41,42]. The iron chalcogenide $AFe_{2-x}Se_2$ belongs to the last category, and many theories based on weak-coupling approaches have suggested d-wave pairing symmetry as possibly detectable through characteristic impurity scattering [43–45].

A complementary approach based on strong coupling likewise predicts an s-wave pairing symmetry in the iron pnictides. Two of us showed that the pairing symmetry is determined mainly by the next-nearest-neighbor (NNN) antiferromagnetic (AFM) exchange coupling J_2 together with a

renormalized narrow band width [11,46]. The superconducting gap is close to a $\cos(k_x)\cos(k_y)$ form in momentum space. (Higher harmonic contributions are neglected in this approach.) This result is model independent as long as the dominating interaction is J_2 and the Fermi surfaces are located close to the Γ and M points in the folded BZ. The $\cos(k_x)\cos(k_y)$ form factor changes sign between the electron and hole pockets in the BZ. It resembles the order parameters of $s^{\pm}$ proposed from weak-coupling arguments [14].

The J_2 coupling will be of particular importance in the following discussion. We make two key points about J_2-related physics as it has appeared in the literature up to now. First, the effect of J_2 is underestimated in most analytic models constructed based on the pure iron lattice with only on-site interactions, since the J_2 exchange coupling originates mostly from superexchange processes through As (P) or Se (Te). Second, one can see that, in our effective model, similar to that used before [11], the strength of the exchange can be as large as $1/4$ of the bandwidth, inducing superconducting gaps of the order of 0.1 eV, which is inconceivably large. In fact, such a strength is inconsistent with numerical evaluations of exchange interactions. However, one should bear in mind that, in the presence of interactions, kinetic energy is suppressed through a Gutzwiller projection. Presumably, the hopping parameter t's are renormalized such that they become comparable to spin exchange, and all explicit values of energy should thus be scaled down by a certain factor (not evaluated in this work). This rescaling factor should be smaller than that for cuprate high-T_c superconductors (SC's), as the interaction strength in iron-based SC's is supposed to be intermediate, i.e., not as large as in cuprates and not as weak as in normal metals.

Comparing the predictions from the weak-coupling and strong-coupling approaches, we find the 122 iron chalcogenides provide an interesting opportunity to address the difference between the two perspectives. In this paper, we predict that the s-wave pairing symmetry is robust even in highly electron-overdoped iron chalcogenides because the AFM J_2 is the main factor for pairing, and the J_1 is assumed to be ferromagnetic (FM), a hypothesis supported by both neutron-scattering experiments [47–50] and the magnetic structure associated with 245 vacancy ordering [51,52]. ("245 vacancy pairing" is the ordering of vacancies of iron atoms into a certain pattern observed in stoichiometric $A_{0.8}Fe_{1.6}As_2$, where A is an alkaline metal.) As we will show, the FM J_1 significantly reduces the competitiveness of d-wave pairing symmetry. We substantiate this claim using two different methods. First, we solve the three-orbital $\{\tilde{t}\}$-J_1-J_2 model on the mean-field level to show that, given large J_2, the s-wave pairing is the leading instability regardless of the change of doping. We calculate the full phase diagram as J_1 varies from FM to AFM. If J_1 is AFM, we obtain a SC state with mixed s- and d-wave pairing in a large range of J_1 values. Second, we use the functional renormalization group (FRG) to analyze this trend obtained by mean-field analysis for a five-band model of the chalcogenides. We confirm that a dominant AFM J_2 generally leads to robust s-wave pairing, while an AFM J_1 tends to favor d-wave pairing in the electron-overdoped region. The competition between s- and d-wave pairing weakens the superconducting instability scale. In addition, it drives the anisotropy features of the superconducting form factor, as consistently obtained for various weak-coupling approaches. As an aside, it has been argued from the weak-coupling picture that the s- and d-wave competition brings about the gap anisotropy or even accidental nodes on the electron pockets around the M point in the folded BZ, i.e., a gap structure that is a compromise between two competing pairing channels [41,53]. In sum, our analysis provides an explanation for the different behavior of superconductivity in the iron pnictides and iron chalcogenides in the electron-overdoped region, as J_1 has the opposite sign for these two classes of materials. (J_1 is AFM in the iron pnictides [54,55] and FM in the iron chalcogenides.) Our study hence suggests that determining the pairing symmetry of the 122 iron chalcogenides can provide important insight regarding whether the local AFM exchange couplings are responsible for the high superconducting transition temperatures.

The paper is organized as follows. In Sec. II, we present the mean-field analysis of the $\tilde{t}$-J_1-J_2 model to show the differences between the iron pnictide setup $J_1 > 0$ and the chalcogenide setup $J_1 < 0$ in the electron-overdoped regime. This is followed by FRG studies in Sec. III, where we investigate the competition between s- and d-wave pairing in the effective model and also analyze the possible effect of an additional pocket at the Γ point of the unfolded BZ, which we find to further increase the robustness of the s-wave pairing. The qualitative trends confirm the results obtained in Sec. II. In Sec. IV, we provide a combined view of the chalcogenides and point out that the ferromagnetic sign of J_1 is important for explaining the robustness of s-wave pairing symmetry in these compounds. Furthermore, we set our work in the context of other approaches to the problem. We conclude in Sec. V that electron-overdoped chalcogenides exhibit a robust s-wave pairing phase when the NNN interactions are correctly taken into account.

II. MEAN-FIELD ANALYSIS

In this section, we use an effective three-orbital model to perform our mean-field analysis for AFe_2Se_2. The model is obtained by modifying a previous three-orbital model in Ref. [56], as previously proposed for iron pnictides. The reasons to use this model rather than a four- or five-orbital model are as follows: (i) as with iron pnictides, the orbital weight of the bands near Fermi surfaces of AFe_2Se_2 is dominated by the d_{xz}, d_{yz}, and d_{xy} orbitals; (ii) one can take advantage of more analytic tractability in a three-orbital model than in a four- or five-orbital model; (iii) there is no qualitative difference between results

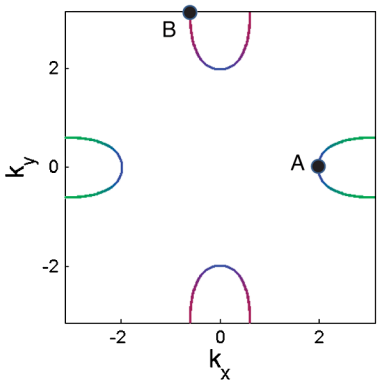

FIG. 1. The Fermi-surface setup used to represent the chalcogenides in the mean-field calculation. Colors indicate the orbital components: red (d_{xz}), green (d_{yz}), and blue (d_{xy}). The areas of blended colors are a reflection of hybridization between orbitals. The A and B points are auxiliary labels used in Figs. 2, 3, and 6.

derived from different models with respect to pairing symmetries and phase diagrams. A more thorough discussion of these aspects can be found in Sec. III.

We specify our model as

$$\hat{T}(k) = \begin{pmatrix} T_{11}(k) - \mu & T_{12}(k) & T_{13}(k) \\ T_{21}(k) & T_{22}(k) - \mu & T_{23}(k) \\ T_{31}(k) & T_{32}(k) & T_{33}(k) - \mu \end{pmatrix}, \quad (1)$$

where

$$\begin{aligned} T_{11}(k) &= 2t_2\cos(k_x) + 2t_1\cos(k_y) + 4t_3\cos(k_x)\cos(k_y), \\ T_{22}(k) &= 2t_1\cos(k_x) + 2t_2\cos(k_y) + 4t_3\cos(k_x)\cos(k_y), \\ T_{33}(k) &= 2t_5[\cos(k_x) + \cos(k_y)] + 4t_6\cos(k_x)\cos(k_y) + \delta, \\ T_{12}(k) &= 4t_4\sin(k_x)\sin(k_y), \\ T_{13}(k) &= 2it_7\sin(k_x) + 4it_8\sin(k_x)\cos(k_y), \\ T_{23}(k) &= 2it_7\sin(k_y) + 4it_8\sin(k_y)\cos(k_x). \end{aligned} \quad (2)$$

The other off-diagonal matrix elements are given by hermiticity. The parameters in the model are taken to be $t = (0.01, 0.05, 0.02, -0.01, 0.2, 0.2, -0.2, 0.1)$, $\delta = 0.4$, and $\mu = 0.312$. (Throughout the article, energies are given in units of eV unless stated otherwise.) The chosen parameter set gives the Fermi surface shown in Fig. 1 with a filling factor of 4.23 electrons per site. The main features are the large electron pockets at X and Y (see Fig. 1), which match the Fermi surfaces observed in ARPES [5–7]. The interaction part in our mean-field calculation is the pairing energy obtained by decoupling the magnetic exchange couplings [11], which can be written as

$$\begin{aligned} \hat{V} = -\sum_{\alpha,\beta,r} (&J_1 b^\dagger_{\alpha,r,r+x} b_{\beta,r,r+x} + J_1 b^\dagger_{\alpha,r,r+y} b_{\beta,r,r+y} \\ &+ J_2 b^\dagger_{\alpha,r,r+x+y} b_{\beta,r,r+x+y} + J_2 b^\dagger_{\alpha,r,r+x-y} b_{\beta,r,r+x-y}), \end{aligned} \quad (3)$$

where $b_{\alpha,r,r'} = c_{\alpha,r,\uparrow}c_{\alpha,r',\downarrow} - c_{\alpha,r,\downarrow}c_{\alpha,r',\uparrow}$ represents singlet pairing operators between the r and r' sites.

There are 12 intraorbital and 12 interorbital pairing parameters when the pairings between two NN and two NNN sites are considered: six possible orbital combinations (three intraorbital plus three interorbital pairings) multiplied by four counted from the NN pairings along (0,1) and (1,0) directions in the square lattice and the NNN pairings along (1,1) and (1, − 1) directions. Because of the multiorbital nature, the one-dimensional representations of the D_{4h} group do not provide a complete classification of all pairing symmetries. As in Ref. [56], one notices that in momentum space, the pairing function decomposes into a k-dependent form factor $f(k)$ and a 3×3 matrix M. The definition of the 24 pairing order parameters is given in Table I, classified by their corresponding one-dimensional irreducible representations of the D_{4h} group. These parameters also have expressions in terms of real space pairings, but for the purposes of this paper, we need only

TABLE I. Definitions of superconducting order parameters and their corresponding irreducible representations and functional forms in momentum space.

Intraorbital pairings			Interorbital pairings		
Symbol	Symmetry	$\hat{f}_\Delta(k)$	Symbol	Symmetry	$\hat{f}_\Delta(k)$
$\Delta^{\mathrm{NN},1}_{\mathrm{intra}}$	A_{1g}	$[\cos(k_x) + \cos(k_y)]\lambda_1/2$	$\Delta^{\mathrm{NN},1}_{\mathrm{inter}}$	A_{2g}	$[\cos(k_x) - \cos(k_y)]\lambda_4$
$\Delta^{\mathrm{NN},2}_{\mathrm{intra}}$	A_{1g}	$[\cos(k_x) - \cos(k_y)]\lambda_2/2$	$\Delta^{\mathrm{NN},2}_{\mathrm{inter}}$	A_{2g}	$\sin(k_x)\lambda_5 - \sin(k_y)\lambda_6$
$\Delta^{\mathrm{NNN},1}_{\mathrm{intra}}$	A_{1g}	$[\cos(k_x + k_y) + \cos(k_x - k_y)]\lambda_1/2$	$\Delta^{\mathrm{NN},3}_{\mathrm{inter}}$	A_{1g}	$\sin(k_x)\lambda_6 + \sin(k_y)\lambda_5$
$\Delta^{\mathrm{NNN},2}_{\mathrm{intra}}$	A_{2g}	$[\cos(k_x - k_y) - \cos(k_x + k_y)]\lambda_2/2\tan$	$\Delta^{\mathrm{NNN},1}_{\mathrm{inter}}$	A_{2g}	$[\cos(k_x + k_y) - \cos(k_x - k_y)]\lambda_4$
$\Delta^{\mathrm{NN},3}_{\mathrm{intra}}$	A_{1g}	$[\cos(k_x) + \cos(k_y)]\lambda_3$	$\Delta^{\mathrm{NNN},2}_{\mathrm{inter}}$	A_{2g}	$\sin(k_x + k_y)(\lambda_5 - \lambda_6)/2 - \sin(k_y - k_x)(\lambda_5 + \lambda_6)/2$
$\Delta^{\mathrm{NNN},3}_{\mathrm{intra}}$	A_{1g}	$[\cos(k_x + k_y) + \cos(k_x - k_y)]\lambda_3$	$\Delta^{\mathrm{NNN},3}_{\mathrm{inter}}$	A_{1g}	$\sin(k_x + k_y)(\lambda_5 + \lambda_6)/2 - \sin(k_y - k_x)(\lambda_5 - \lambda_6)/2$
$\Delta^{\mathrm{NN},4}_{\mathrm{intra}}$	B_{1g}	$[\cos(k_x) + \cos(k_y)]\lambda_2/2$	$\Delta^{\mathrm{NN},4}_{\mathrm{inter}}$	B_{2g}	$[\cos(k_x) + \cos(k_y)]\lambda_4$
$\Delta^{\mathrm{NN},5}_{\mathrm{intra}}$	B_{1g}	$[\cos(k_x) - \cos(k_y)]\lambda_1/2$	$\Delta^{\mathrm{NN},5}_{\mathrm{inter}}$	B_{2g}	$\sin(k_x)\lambda_5 + \sin(k_y)\lambda_6$
$\Delta^{\mathrm{NNN},4}_{\mathrm{intra}}$	B_{1g}	$[\cos(k_x + k_y) + \cos(k_x - k_y)]\lambda_2/2$	$\Delta^{\mathrm{NN},6}_{\mathrm{inter}}$	B_{1g}	$\sin(k_x)\lambda_6 - \sin(k_y)\lambda_5$
$\Delta^{\mathrm{NNN},5}_{\mathrm{intra}}$	B_{2g}	$[\cos(k_x - k_y) - \cos(k_x + k_y)]\lambda_1/2\cosh$	$\Delta^{\mathrm{NNN},4}_{\mathrm{inter}}$	B_{2g}	$[\cos(k_x + k_y) + \cos(k_x - k_y)]\lambda_4$
$\Delta^{\mathrm{NN},6}_{\mathrm{intra}}$	B_{1g}	$[\cos(k_x) - \cos(k_y)]\lambda_3\log$	$\Delta^{\mathrm{NNN},5}_{\mathrm{inter}}$	B_{2g}	$\sin(k_x + k_y)(\lambda_5 + \lambda_6)/2 + \sin(k_y - k_x)(\lambda_5 - \lambda_6)/2$
$\Delta^{\mathrm{NNN},6}_{\mathrm{intra}}$	B_{2g}	$[\cos(k_x - k_y) - \cos(k_x + k_y)]\lambda_3\cosh$	$\Delta^{\mathrm{NNN},6}_{\mathrm{inter}}$	B_{1g}	$\sin(k_x + k_y)(\lambda_5 - \lambda_6)/2 + \sin(k_y - k_x)(\lambda_5 + \lambda_6)/2$

the functional forms in momentum space. In Table I, the λ_i's $(i = 1, \ldots, 6)$ are likewise 3×3 matrices, whose definitions are given in the Appendix.

In reciprocal-lattice space, the mean-field Hamiltonian is given by

$$\hat{H} = \sum_k \begin{pmatrix} \hat{T}(k) & \hat{\Delta}(k) \\ \hat{\Delta}^\dagger(k) & -\hat{T}^\star(-k) \end{pmatrix}, \tag{4}$$

where

$$\hat{\Delta}(k) = \sum_{i=1,\ldots,6} \Delta_{\text{intra}}^{\text{NN},i} \hat{f}_{\Delta_{\text{intra}}^{\text{NN},i}}(k) + \Delta_{\text{intra}}^{\text{NNN},i} \hat{f}_{\Delta_{\text{intra}}^{\text{NNN},i}}(k) + \Delta_{\text{inter}}^{\text{NN},i} \hat{f}_{\Delta_{\text{inter}}^{\text{NN},i}}(k) + \Delta_{\text{inter}}^{\text{NNN},i} \hat{f}_{\Delta_{\text{inter}}^{\text{NNN},i}}(k). \tag{5}$$

The zero-temperature free energy in terms of the order parameters is given by

$$F(\{\Delta\}) = -2\sum_k \sum_{i=1,2,3} E_i(k) + 4\frac{\sum_{i=1,2,4,5} |\Delta_{\text{intra}}^{\text{NN},i}|^2 + \sum_{i=3,6} |\Delta_{\text{intra}}^{\text{NN},i}|^2/2 + \sum_{i=1,\ldots,6} |\Delta_{\text{inter}}^{\text{NN},i}|^2/2}{J_1} + 4\frac{\sum_{i=1,2,4,5} |\Delta_{\text{intra}}^{\text{NNN},i}|^2 + \sum_{i=2,3,5,6} |\Delta_{\text{inter}}^{\text{NNN},i}|^2 + \sum_{i=3,6} |\Delta_{\text{intra}}^{\text{NN},i}|^2/2 + \sum_{i=1,4} |\Delta_{\text{inter}}^{\text{NN},i}|^2/2}{J_2}. \tag{6}$$

By minimizing this free energy with respect to $\{\Delta\}$, we can derive the self-consistent equations to obtain the pairing symmetries and the associated phase diagram. In general, there is more than one self-consistent solution for $\{\Delta\}$. The solutions represent local minima of the free energy. The free energies of these solutions hence must be compared to find the global minimum, i.e., the ground state.

First, we fix $J_1 = 0$ and consider pure NNN pairings stemming from J_2. We take J_2 from 0 to 1.5 for a bandwidth $W \sim 4$. All nonzero SC order parameters (intra- and interorbital) are plotted against parameter J_2 in Fig. 2(a). The robust SC solution with a purely A-type s-wave pairing is obtained when J_2 is larger than 0.4. In this case, the pairing remains the same as that in iron pnictides, with the geometric factor $\cos(k_x)\cos(k_y)$ [11]. The Bogoliubov particle spectrum is completely gapped in this state. The quasiparticle spectrum is anisotropic along the Fermi surface (FS), because the pairing of the d_{xy} orbital ($\Delta_{\text{intra}}^{\text{NNN},3}$) is about one-half of the pairings of d_{xz}, d_{yz} orbitals ($\Delta_{\text{intra}}^{\text{NNN},1}$). When J_2 becomes larger than 1, the ground state is a mixture of A-type and B-type pairings. The leading B-type pairing corresponds to $\Delta_{\text{intra}}^{\text{NNN},5}$ with a form factor of $\sin(k_x)\sin(k_y)$. In the coexisting phase, the quasiparticle spectra become more anisotropic and their dispersions explicitly break C_4 rotation symmetry, as shown in Fig. 2(c). The intraorbital pairings are found to be significantly larger than the interorbital ones throughout the parameter region, similar to the case of pnictides [11]. The gaps associated with the d_{xy} orbital are found to be smaller than those with d_{xz}, d_{yz} orbitals.

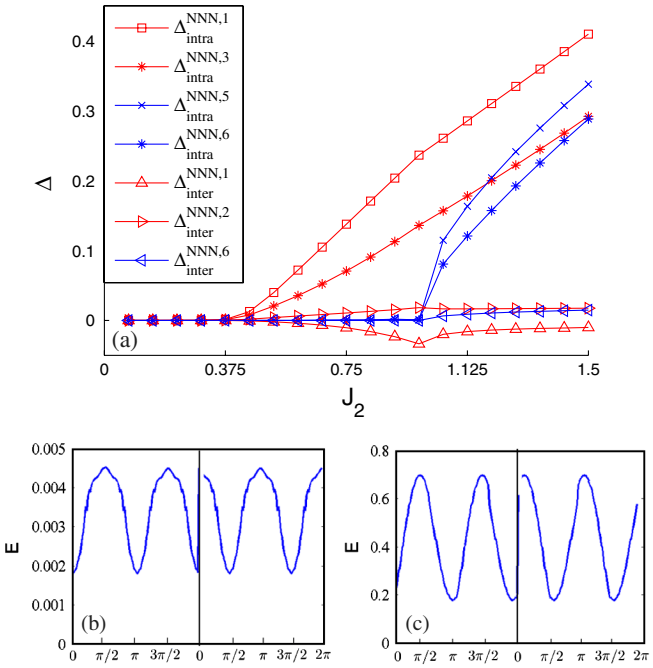

FIG. 2. (a) Mean-field phase diagram along $J_1 = 0$ in parameter space. Size of the gap around Fermi surfaces at (b) $J_2 = 0.4$ and (c) $J_2 = 1.5$. In the left half of (b) and (c), the k point traces the electron pocket around the X point counterclockwise from point A in Fig. 1, while in the right half it traces the electron pocket around the Y point counterclockwise from point B in Fig. 1.

Second, we study the phase diagram when only (antiferromagnetic) J_1 is present. All nonzero SC order parameters are plotted against J_1 in Fig. 3(a). We increase J_1 from 0 to 1.5 and take the bandwidth $W \sim 4$. The SC order parameter becomes nonzero from $J_1 \sim 0.35$. Between $J_1 = 0.35$ and $J_1 = 0.5$, the nonzero order components are $\Delta_{\text{intra}}^{\text{NN},5}$, $\Delta_{\text{intra}}^{\text{NN},6}$, and $\Delta_{\text{inter}}^{\text{NN},5} = \Delta_{\text{inter}}^{\text{NN},6}$, all having B-type symmetry. In this parameter range, the quasiparticle spectrum is completely gapped with almost isotropic gaps. As soon as $J_1 > 0.5$, A-type symmetry order parameters become nonzero and coexist with B-type order parameters. The leading order parameters in the mixed phase are $\Delta_{\text{intra}}^{\text{NN},1}$, $\Delta_{\text{intra}}^{\text{NN},3}$, $\Delta_{\text{intra}}^{\text{NN},5}$, and $\Delta_{\text{intra}}^{\text{NN},6}$. Because of strong mixing of A- and B-type pairings, the quasiparticle spectrum is anisotropic [Fig. 3(c)]. It is, however, still nodeless, in contrast to a pure s-wave pairing $\cos(k_x) + \cos(k_y)$ where there are nodes [39] on the electron pockets. Moreover,

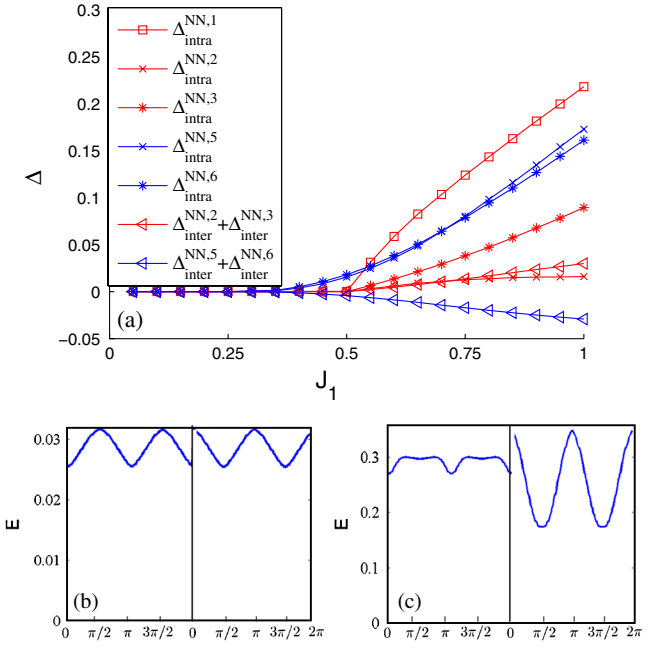

FIG. 3. (a) Mean-field phase diagram along $J_2 = 0$ in the parameter space. Size of the gap around the Fermi surfaces at (b) $J_1 = 0.5$ and (c) $J_1 = 1$. The k-point traces are defined as in Fig. 2.

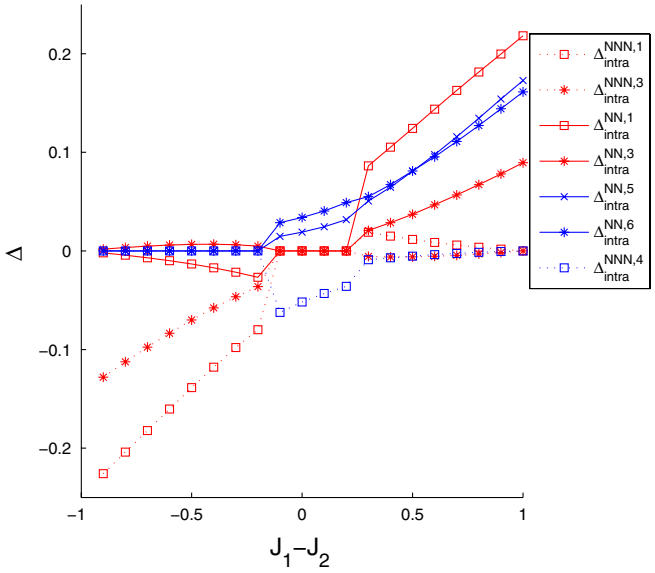

FIG. 4. Mean-field phase diagram as a function of $J_1 - J_2$ along $J_1 + J_2 = 1$ in parameter space.

the C_4 symmetry is again explicitly broken in the spectrum of the coexisting phase. The dominant pairings are still intraorbital pairings. When J_1 is large, however, the interorbital components $\Delta^{\mathrm{NN},5}_{\mathrm{inter}} = \Delta^{\mathrm{NN},6}_{\mathrm{inter}}$ also become significant.

Finally, when both J_1 and J_2 are antiferromagnetic, we fix $J_1 + J_2 = 1$ and change $J_1 - J_2$ as a parameter. We observe that NNN pairings dominate for $J_1 - J_2 < -0.1$ and NN pairings dominate for $J_1 - J_2 > 0.2$ (Fig. 4). In the intermediate range, there are only weak B-type pairings. A schematic phase diagram within the range $0 < J_1, J_2 < 1$ is shown in Fig. 5.

In the entire parameter region of (J_1, J_2), the SC order parameters always have the same sign for all three orbitals. This can be seen in Fig. 6, where the orbital-resolved pairing amplitude is shown along electron pockets around X. This result is consistent with the FRG result shown in Sec. III (Fig. 12). It is, however, different from the result in the very-strong-coupling limit in Ref. [57], where the strong interorbital repulsion favors different signs between the d_{xy} intraorbital and the d_{xz}, d_{yz} intraorbital pairings. Some quantitative differences between Figs. 6 and 12 may be explained due to the incompleteness of a three-orbital model. Figure 6 also shows that the orbital-resolved pairing amplitude is highly anisotropic: this is a natural reflection of orbital character differences on different parts of the Fermi surface.

The above results are obtained only for a band structure that has electron pockets. For completeness of the analysis, we have also adapted the parameters such that an additional electron pocket around the M point appears; it would map to the Γ point in a folded BZ. Such a band structure is of realistic interest, as ARPES experiments have observed a small pocket at Γ in the folded BZ. In this case, our calculation shows that s-wave pairings are more favored than in the previous case because the geometric factors of choice, i.e., $\cos(k_x)\cos(k_y)$ or $\cos(k_x) + \cos(k_y)$, are both maximized around M. With the three-pocket FS, taking $J_1 = 0$ and increasing $J_2 > 0$, B-type pairings blend in at larger J_2, as shown in Fig. 2(a). Taking $J_2 = 0$ and increasing $J_1 > 0$, A-type pairings appear at slightly smaller J_1 than are shown in Fig. 3(a). Still, the main features remain unchanged. These trends are in accordance with the FRG studies as discussed in the following section.

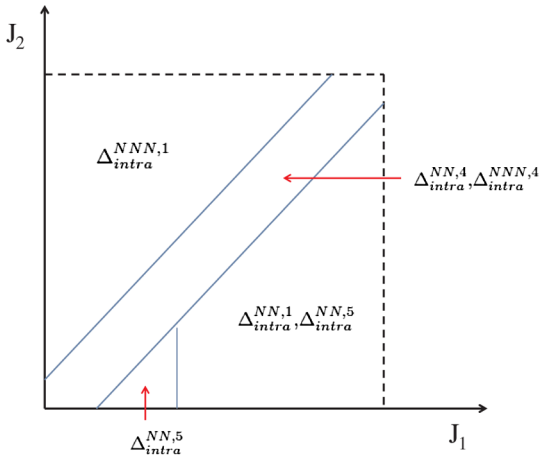

FIG. 5. Schematic phase diagram for the model (4) within $0 < J_2, J_2 < 1$.

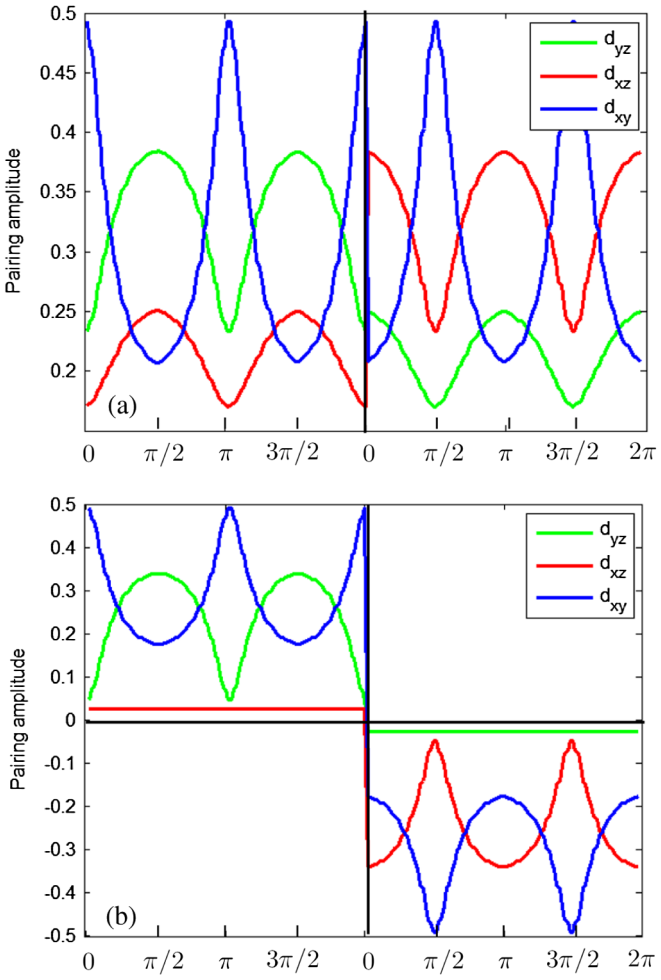

FIG. 6. The orbital-resolved pairing amplitude on the FS for a typical s-wave/d-wave pairing state in the upper and lower panels, calculated within mean-field approximation. The interaction parameters are $J_1 = 0$, $J_2 = 0.8$ for the upper panel and $J_1 = 0.5$, $J_2 = 0$ for the lower panel. The k point traces are defined as in Fig. 2.

III. FUNCTIONAL RENORMALIZATION-GROUP ANALYSIS

To substantiate the mean-field results described above, we employ functional renormalization-group analysis [58–60] to further investigate the pairing symmetry of the $\tilde{t}$-J_1-J_2 model. As an unbiased resummation scheme of all channels, the FRG has been extended and fully employed to the multiband case of iron pnictides. More details can be found in Refs. [13,17,39,61]. The conventional starting point for the FRG is the bare Hubbard-type interaction, which develops different Fermi-surface instabilities as higher momenta are integrated out when the cutoff of the theory flows to the Fermi surface. To address the special situation found in the chalcogenides where the Fe-Se coupling is strong, not only local but also further-neighbor interaction terms would have to be taken into account: in our FRG setup, the onsite Hubbard-type interactions of the same type as used in the study of pnictides trigger no instability at reasonable critical scales. This result already at this stage suggests that the chalcogenides may necessitate a perspective beyond pure weak coupling. In addition, the total parameter space of bare interactions is large, and constrained random-phase approximation parameters are not yet available for this class of materials. For the purpose of our study, we hence constrain ourselves to the $\tilde{t}$-J_1-J_2 model from the outset. This implies that the pairing interaction is already attractive on the bare-interaction level, and a development of a SC instability is expected as the physics is dominated by the pairing channel. Still, we can employ the FRG method to investigate the properties and competition of different SC pairing symmetries for the chalcogenides for different (J_1,J_2) regimes.

Within the FRG approach, we consider general J_1-J_2 interactions that are not limited to the spins in the same orbital:

$$H = J_1 \sum_{\langle i,j\rangle} \sum_{a,b} \left(\mathbf{S}_{ia} \cdot \mathbf{S}_{jb} - \frac{1}{4} n_{ia} n_{jb} \right) + J_2 \sum_{\langle\langle i,j\rangle\rangle} \sum_{a,b} \left(\mathbf{S}_{ia} \cdot \mathbf{S}_{jb} - \frac{1}{4} n_{ia} n_{jb} \right).$$

The kinetic theory will differ in the various cases studied below. For all cases, we will study the full five-band model incorporating all Fe d orbitals. Concerning the discretization of the BZ, the renormalization-group (RG) calculations were performed with 8 patches per pocket, and a $10_{\text{radius}} \times 3_{\text{angle}}$ mesh on each patch. (This moderate resolution is convenient for scanning wide ranges of the interaction parameter space; we checked that increasing the BZ resolution did not qualitatively change our findings.) The output of the RG calculation is the four-point vertex on the Fermi surfaces,

$$V_\Lambda(\mathbf{k}_1, n_1; \mathbf{k}_2, n_2; \mathbf{k}_3, n_3; \mathbf{k}_4, n_4) c^\dagger_{\mathbf{k}_4 n_4 s} c^\dagger_{\mathbf{k}_3 n_3 \bar{s}} c_{\mathbf{k}_2 n_2 s} c_{\mathbf{k}_1 n_1 \bar{s}},$$

where the flow parameter is the IR cutoff Λ approaching the Fermi surface, and $\mathbf{k}_1$ to $\mathbf{k}_4$ are the incoming and outgoing momenta. We find only singlet pairing to be relevant for the scenarios that we studied:

$$\sum_{\mathbf{k},\mathbf{p}} V_\Lambda(\mathbf{k}, \mathbf{p}) [\hat{O}^\dagger_{\mathbf{k}} \hat{O}_{\mathbf{p}}],$$

where $\hat{O}^{\text{SC}}_{\mathbf{k}} = c_{\mathbf{k},\uparrow} c_{-\mathbf{k},\downarrow}$. We decompose the pairing channel into eigenmodes,

$$V^{\text{SC}}_\Lambda(\mathbf{k}, -\mathbf{k}, \mathbf{p}) = \sum_i c^{\text{SC}}_i(\Lambda) f^{\text{SC},i}(\mathbf{k})^* f^{\text{SC},i}(\mathbf{p}), \qquad (7)$$

and obtain the band-resolved form factors of the leading and subleading SC eigenmode (i.e., the largest two negative eigenvalues). Having done so, we are able to discuss the interplay of d- and s-wave pairings as well as the degree of form-factor anisotropy for a given setting of

(J_1-J_2). Comparing divergence scales Λ_c gives us the possibility to investigate the relative change of T_c as a function of (J_1-J_2). Furthermore, we also investigate the orbital-resolved pairing modes [39] by decomposing the orbital four-point vertex

$$V^{\mathrm{orb}}_{c,d\to a,b} = \sum_{n_1,\ldots,n_4=1}^{5} \{V_\Lambda(\mathbf{k}_1, n_1; \mathbf{k}_2, n_2; \mathbf{k}_3, n_3; \mathbf{k}_4, n_4) u^*_{an_1} \times (\mathbf{k}_1) u^*_{bn_2}(\mathbf{k}_2) u_{cn_3}(\mathbf{k}_3) u_{dn_4}(\mathbf{k}_4)\}, \quad (8)$$

where the u's denote the different orbital components of the band vectors. By investigating the intraorbital SC pairing modes in (8), we make contact with the findings from the previous mean-field analysis.

A. Two-pocket scenario

We start by studying the five-band model suggested by Maier *et al.* [44]. There are only two electron pockets at the X point of the unfolded Brillouin zone closely resembling the Fermi-surface topology and orbital content employed for our mean-field analysis (Fig. 7).

The RG flow and the form factors of the leading diverging channels are shown in Fig. 8 for dominant J_2 and in Fig. 9 for dominant J_1. As stated before, the pairing interaction is already present at the bare level in the model so that we achieve comparably fast instabilities as the cutoff is flowing toward the Fermi surface. As found in Ref. [11], the dominant J_2 scenario exhibits a leading s-wave $\cos(k_x)\cos(k_y)$ form factor, which causes the same sign on both electron pockets (blue dots in Fig. 8). The subleading form factor is found to be of d-wave $\cos(k_x) - \cos(k_y)$ type, changing sign from one electron pocket to the other. The inverse situation is found for dominant J_1. As shown in Fig. 9, the d-wave $\cos(k_x) - \cos(k_y)$ form factor establishes the leading instability. As before, the form factor does not cross zero as related to the nodeless SC for this parameter setting.

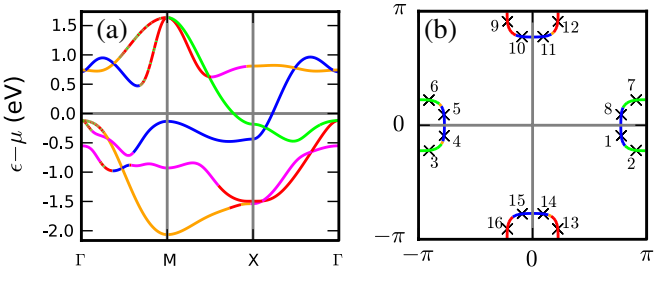

FIG. 7. The spectrum (a) and the Fermi surfaces (b) of the band structure proposed by Maier *et al.* [44], colored according to the dominant orbital content. The color code is red, (d_{xz}); green, (d_{yz}); blue, (d_{xy}); orange, ($d_{x^2-y^2}$); and magenta, ($d_{3z^2-r^2}$). The numbered crosses in (b) show the center of Fermi surface patches used in the FRG calculations.

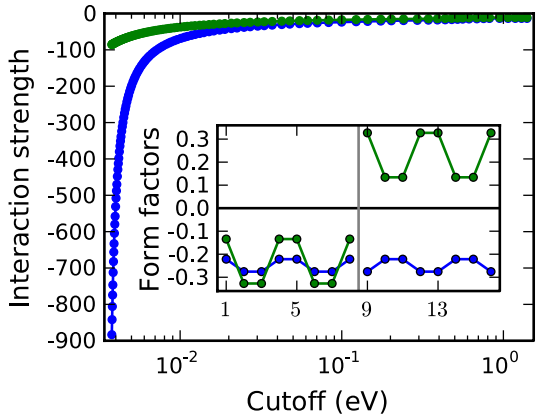

FIG. 8. Typical RG flows and the superconducting gaps associated with the Fermi surfaces for the two-pocket scenario with (J_1,J_2) = (0.1, 0.5) eV. Leading form factor is denoted in blue, subleading form factor in green.

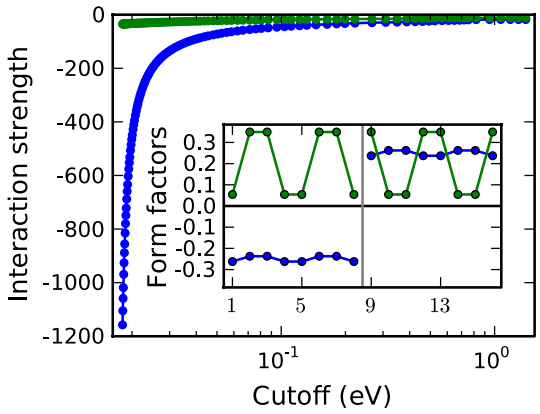

FIG. 9. Typical RG flows and the superconducting gaps associated with the Fermi surfaces for the two-pocket scenario with (J_1,J_2) = (0.5, 0.1) eV. Leading form factor is denoted in blue, subleading form factor in green.

With pairing information available only on the limited number of sampling points along FS, it is impossible to extract all 24 order parameters (or, more strictly, 24 different instabilities) defined in Sec. II. For illustration, a mixture of a small A-type NNN d-wave pairing and a large A-type NNN s-wave pairing is indistinguishable from a pure A-type NNN s-wave pairing. A mixed state of a small B-type NN s-wave pairing plus a large B-type NN d-wave pairing, and a state with pure B-type NN d-wave pairing show little difference if one compares the gap on a few points along the Fermi surfaces. For this reason, the symbol $s_{x^2y^2}$ used in this section refers to a pairing consisting of a large A-type NNN s-wave pairing and possible small components of A-type NNN d-wave pairing or A-type NN s/d-wave pairing. In turn, the symbol $d_{x^2-y^2}$ refers to a pairing made up of a large B-type NN d-wave pairing and possible small components of B-type NN s-wave pairing or B-type NNN s- or d-wave pairing.

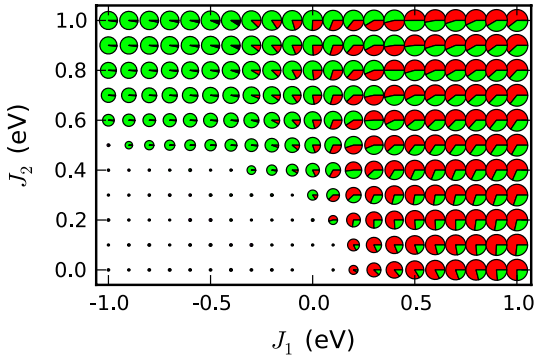

FIG. 10. The phase diagram of the two-pocket model. The variation with (J_1,J_2) of the critical scale Λ_c and the competition between the s and d waves are depicted by the array of pie charts. In each pie, the two sectors denote the two leading pairing channels (the $s_{x^2y^2}$-wave pairing in green and the $d_{x^2-y^2}$-wave pairing in red), with the angle of each sector proportional to pairing strength. The size of each pie reflects the critical scale Λ_c, with its radius proportional to $[\log_{10}(\Lambda_c/10^{-8}\ \text{eV})]^2$.

We have scanned a large range of (J_1,J_2). For each setup, we obtain Λ_c as well as the ratio of the instability eigenvalues between s and d waves in the pairing channel (encoded by the two-color circles shown in Fig. 10). The FRG result is qualitatively consistent with the mean-field analysis. In the antiferromagnetic sector, the s-wave pairing wins for dominant J_2, while the d-wave pairing wins for dominant J_1. For ferromagnetic J_1, corresponding to the situation in chalcogenides, we find a robust preference of s-wave pairing. The anisotropy of the s-wave gap around the pockets in the FRG calculation is also qualitatively consistent with the mean-field result. The gap on the Fermi surfaces with d_{xy} orbital character is smaller than the gap on those with d_{xz}, d_{yz} orbital character.

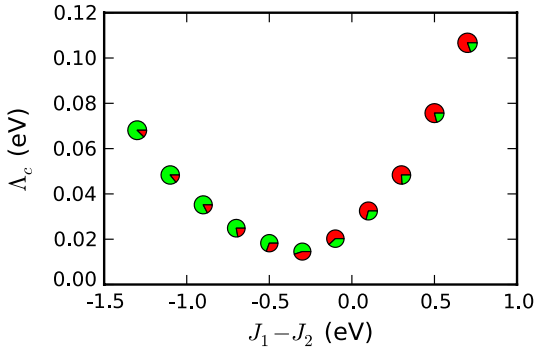

FIG. 11. Variation of the critical scale Λ_c and competition between pairing channels along a line through parameter space which interpolates between the $s_{x^2y^2}$ and $d_{x^2-y^2}$ waves. As described in the caption to Fig. 10, the pairing propensity in each channel is denoted by the angular size of the corresponding sector in the pie chart. A correlation between Λ_c and the competition between channels is observed: Λ_c reaches its minimum when the two channels in competition have comparable ordering tendency.

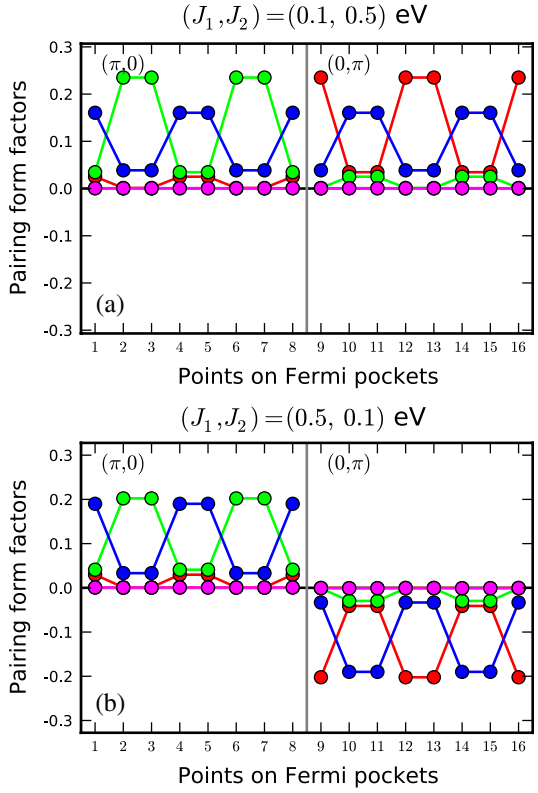

FIG. 12. Orbital-resolved pairing form factors of two typical RG flows. (a) resides in the dominant s-wave regime, (b) in the d-wave regime. The color code is the same as in Fig. 7.

The predictions from the mean-field analysis are further confirmed for the mixed-phase regime where s and d waves coexist in the mean-field solution. In FRG, one of these instabilities will always be slightly preferred; still, when both instabilities diverge in very close proximity to each other, this regime behaves similarly to the coexistence phase. For illustration, in Fig. 11 we have plotted the dependence of Λ_c on J_1-J_2, with J_1+J_2 fixed to 0.7 eV; there is a clear reduction of the critical scale (and thus the transition temperature) when there is strong competition between s- and d-wave channels.

Following (8), we also analyze the orbital decomposition of the SC pairing from FRG (Fig. 12). We constrain ourselves to the most relevant three orbitals d_{xy}, d_{xz}, and d_{yz}. In particular, we observe that the SC orbital pairing induces the same sign for all three dominant orbital modes, in correspondence with the mean-field analysis presented before.

B. Three-pocket scenario

Recent ARPES data [62] on the chalcogenides may suggest the existence of a shallow flat pocket around the Γ point. (The location and especially the k_z position of such a pocket are still under debate.) In the previous section, by using tuning parameters, we obtained a

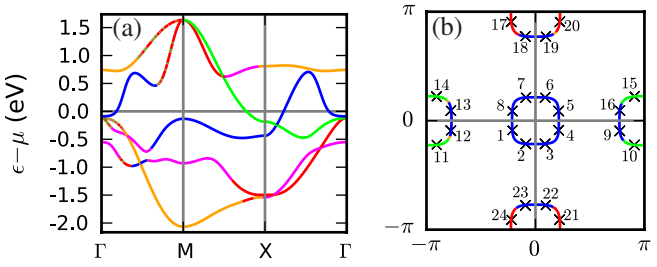

FIG. 13. (a) The band structure and (b) the Fermi surfaces of the modified band structure with an electron pocket added at Γ, colored according to the dominant orbital content. The color code is red, d_{xz}; green, d_{yz}; blue, d_{xy}; orange, $d_{x^2-y^2}$; and magenta, $d_{3z^2-r^2}$. The numbered crosses show the center of Fermi-surface patches used in the FRG calculations.

three-orbital model that has an additional electron pocket around the M point in the unfolded BZ.

In our FRG approach, we can take a more profound microscopic perspective on this issue. From the true band-structure calculations at hand for the chalcogenides, we consider it unlikely that it will be a hole band regularized up toward the Fermi surface.

Instead, we investigate the effect of a possible electron band at the Γ point in the unfolded Brillouin zone. This approach is suggested from the folded 10-band calculations, where one electron-type band closely approaches the Fermi level around the Γ point [44]. This band should be very flat and shallow. From the weak-coupling perspective of particle-hole pairs created around the Fermi surfaces, this will probably have a small effect: particle-hole pairs will be created only up to energy scales of the depth of the electron band at the X point below the Fermi surface, providing some hole-type phase space for the electron band at Γ. In a (J_1,J_2) picture, however, this effect may still significantly promote scattering along $\Gamma \leftrightarrow X$,

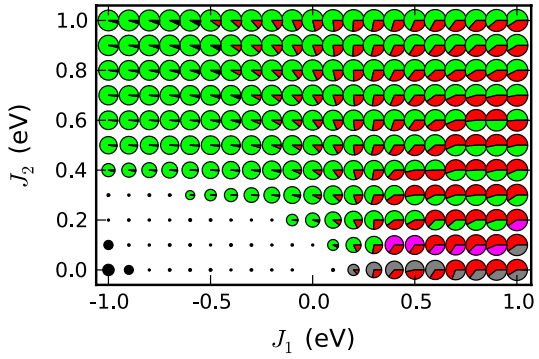

FIG. 14. The phase diagram of the three-pocket model. Here we are able to resolve the s-wave channel into constant s wave (gray), extended $s_{x^2y^2}$ wave (green), and the nodal $s_{x^2+y^2}$ wave (purple). See the caption to Fig. 10 for more details on the pie charts. Parameter sets with $J_1 \sim -1$ and $J_2 \sim 0$ have highly oscillating form factors due to artifacts in the calculation; the triplet channel would have to be considered in these cases.

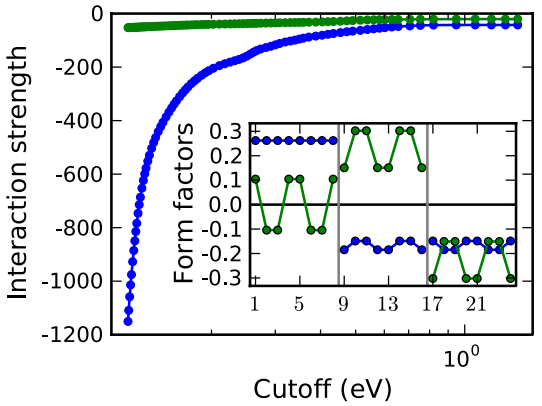

FIG. 15. Typical RG flows and the superconducting gaps associated with FS setup for the three-pocket scenario with $(J_1,J_2) = (0.2, 0.8)$ eV. Leading form factor is denoted in blue, subleading form factor in green.

which may further stabilize the s-wave phase regime. We have hence developed a modified band structure designed for this scenario. There, we have bent down the band dominated by d_{xy} in the two-pocket model band structure [44] without changing its band vector and have created an electron pocket around Γ which is of d_{xy} orbital content (Fig. 13). The band bending was achieved by

$$H \rightarrow H + \sum_{\mathbf{k},a,b,s} \xi(\mathbf{k}) c^{\dagger}_{\mathbf{k}as} u_a(\mathbf{k}) u^{*}_b(\mathbf{k}) c_{\mathbf{k}bs},$$

where $u(\mathbf{k})$ is the eigenvector of the band dominated by d_{xy}. The shift of energy $\xi(\mathbf{k})$ was intentionally chosen such that the Γ pocket exhibits some nesting with the X electron pockets (Fig. 13).

The phase diagram is shown in Fig. 14. FRG results for typical scenarios for the s- and d-wave regimes are shown in Figs. 15 and 16, respectively. As suspected, the additional pocket strengthens the tendency to form

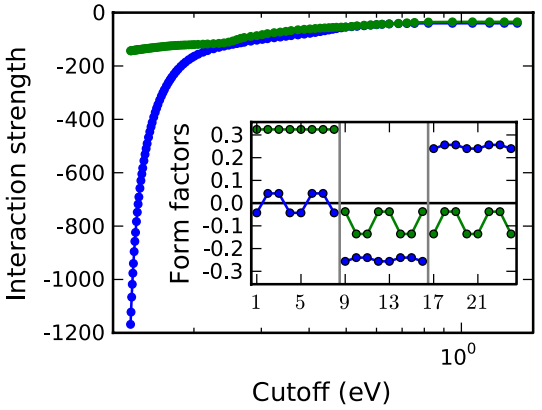

FIG. 16. Typical RG flows and the superconducting gaps associated with FS setup for the three-pocket scenario with $(J_1,J_2) = (0.9, 0.3)$ eV. Leading form factor is denoted in blue, subleading form factor in green.

an s wave in the system, aside from exhibiting an additional constant s-wave instability in a small regime for dominant J_1.

IV. DISCUSSION

The calculations presented above demonstrate that the s-wave pairing symmetry is always robust if the AFM NNN J_2 is strong, while a d-wave pairing can be strong if J_1 is AFM and dominant in size for the electron-overdoped region. Moreover, if both of them are AFM, there is strong competition between the s- and d-wave pairing. When there are hole pockets, as has been shown before [11], even in a range of $J_1 \sim J_2$, the contribution to pairing from J_1 is much weaker than that from J_2. In that case, an AFM J_1 will not generate strong d-wave pairing, and the s-wave pairing wins easily. From neutron-scattering experiments, it has been shown that a major difference between iron pnictides and iron chalcogenides is that the NN coupling J_1 changes from AFM in the former [54,55] to FM in the latter [47]. In fact, J_1 is rather strongly FM in the latter, which explains the high magnetic transition temperature (500 K) in the 245 vacancy ordering state as shown in Ref. [52]. Combining these results, we can partially answer the question regarding the different behaviors between iron pnictides and iron chalcogenides in the electron-overdoped region: why can the high SC transition temperature be achieved in the latter, but not in the former? Since J_1 in iron pnictides is AFM while it is FM in iron chalcogenides, J_1 will weaken the SC pairing in the former but not in the latter.

A few remarks regarding this work follow: (i) Our mean-field result is qualitatively consistent with the results from a similar model with five orbitals [63,64]. The critical difference appears to be regarding J_1 as being FM, which has not been addressed previously. (ii) s-wave pairing symmetry has also been obtained in Refs. [43,65,66]. However, the s-wave pairing only appears either in a narrow region or with drastically different parameter settings. Therefore, the s-wave pairing is not robust from a microscopic point of view. Instead, the d-wave pairing is a robust result in these studies. Still, even the d-wave pairing strength based on the scattering between two electron pockets is generally weak, as specifically discussed in Ref. [63], which is another difficulty for this type of mechanism. (iii) Our results suggest that there is no difference between iron pnictides and iron chalcogenides in terms of pairing symmetry. Both of them are dominated by s-wave pairing. If both hole and electron pockets are present, the signs of the SC order in hole and electron pockets are opposite, namely, $s^{\pm}$. However, the mechanism causing $s^{\pm}$ is different in the weak- and strong-coupling approaches. In the weak-coupling approach, the sign change is due to the scattering between the hole and the electron pockets, while in the strong-coupling approach, the sign change is due to the form factor of the SC order parameters, which is specified to be $\cos(k_x)\cos(k_y)$, since the pairing mainly originates from the AFM J_2 coupling. Therefore, to obtain $s^{\pm}$ pairing symmetry, the existence of both hole and electron pockets is necessary in the weak-coupling approach but not in the strong-coupling one. (iv) The reason that the superconductivity vanishes in the iron pnictides in the electron-overdoped region is not solely due to the competition between s- and d-wave pairing symmetry. It is also due to the weakening of local magnetic exchange couplings themselves and the reduction of band width renormalization. (v) The prospective experimental confirmation of s-wave pairing symmetry in KFe_2Se_2 will support the hypothesis that superconductivity in iron-based superconductors might be explained by local AFM exchange couplings. (vi) Neutron scattering also suggests that there is significant AFM exchange coupling between two third-nearest-neighbor sites, i.e., J_3 [47,49]. The existence of J_3 will further enhance the s-wave pairing, since it generates pairing form factors such as $\cos(2k_x) + \cos(2k_y)$ in reciprocal space, which in turn can enhance the pairing at the electron pockets.

V. CONCLUSION

In summary, we have shown that the pairing symmetry in electron-overdoped iron chalcogenides is a robust s-wave pairing. A ferromagnetic NN exchange coupling diminishes the possibility of d-wave pairing symmetry in these materials. From a unified perspective of high-T_c cuprates and high-T_c chalcogenides, the NN antiferromagnetic exchange coupling gives rise to the robust d-wave pairing in the cuprates, while the NNN AFM exchange coupling gives rise to the robust s-wave pairing in iron-based chalcogenide superconductors.

ACKNOWLEDGMENTS

We thank S. Borisenko, J. van den Brink, Xianhui Chen, A. Chubukov, Hong Ding, Donglei Feng, S. Graser, W. Hanke, P. Hirschfeld, S. Kivelson, C. Platt, D. Scalapino, Qimiao Si, Xiang Tao, Fa Wang, and Haihu Wen for useful discussions. J. P. H. thanks the Institute of Physics, CAS, for research support. R. T. is supported by DFG SPP 1458/1, a Feodor Lynen Fellowship of the Humboldt Foundation, and NSF Contract No. DMR-095242. B. A. B. is supported by Princeton Startup Funds, the Sloan Foundation, NSF Contract No. DMR-095242, NSF China Contract No. 11050110420, and an MRSEC grant at Princeton University, NSF Contract No. DMR-0819860.

APPENDIX: 3 × 3 MATRICES FOR DEFINING SUPERCONDUCTOR ORDER PARAMETERS

For concision in Table I where mean-field gaps are defined, we have used six predefined 3×3 matrices. The definitions are

$$\lambda_1 = \begin{pmatrix} 1 & 0 & 0 \\ 0 & 1 & 0 \\ 0 & 0 & 0 \end{pmatrix}, \quad \lambda_2 = \begin{pmatrix} 1 & 0 & 0 \\ 0 & -1 & 0 \\ 0 & 0 & 0 \end{pmatrix},$$

$$\lambda_3 = \begin{pmatrix} 0 & 0 & 0 \\ 0 & 0 & 0 \\ 0 & 0 & 1 \end{pmatrix}, \quad \lambda_4 = \begin{pmatrix} 0 & 1 & 0 \\ 1 & 0 & 0 \\ 0 & 0 & 0 \end{pmatrix},$$

$$\lambda_5 = \begin{pmatrix} 0 & 0 & i \\ 0 & 0 & 0 \\ -i & 0 & 0 \end{pmatrix}, \quad \lambda_6 = \begin{pmatrix} 0 & 0 & 0 \\ 0 & 0 & i \\ 0 & -i & 0 \end{pmatrix}.$$

[1] J. Guo, S. Jin, G. Wang, S. Wang, K. Zhu, T. Zhou, M. He, and X. Chen, *Superconductivity in the Iron Selenide* $K_xFe_2Se_2$ *(*$0x1.0$*)*, Phys. Rev. B **82**, 180520 (2010).

[2] M. Fang, H. Wang, C. Dong, Z. Li, C. Feng, J. Chen, and H. Q. Yuan, *Fe-based Superconductivity with* $T_c = 31$K *Bordering an Antiferromagnetic Insulator in* (Tl, K)Fe_xSe_2 *Crystals*, Europhys. Lett. **94**, 27009 (2011).

[3] R. H. Liu, X. G. Luo, M. Zhang, A. F. Wang, J. J. Ying, Y. J. Yan, Z. J. Xiang, P. Cheng, G. J. Ye, Z. Y. Li, and X. H. Chen, *Coexistence of Superconductivity and Antiferromagnetism in Single Crystals* $A_{0.8}Fe_{2-y}Se_2$ *(*A = K, Rb, Cs, Tl, K *and* Tl/Rb*): Evidence from Magnetization and Resistivity*, Europhys. Lett. **94**, 27008 (2011).

[4] D. N. Basov and A. V. Chubukov, *Manifesto for a Higher* T_c, Nature Phys. **7**, 272 (2011).

[5] Y. Zhang, L. X. Yang, M. Xu, Z. R. Ye, F. Chen, C. He, H. C. Xu, J. Jiang, B. P. Xie, J. J. Ying, X. F. Wang, X. H. Chen, J. P. Hu, M. Matsunami, S. Kimura, and D. L. Feng, *Nodeless Superconducting Gap in* $A_xFe_2Se_2$ *(*A = K, *Cs) Revealed by Angle-Resolved Photoemission Spectroscopy*, Nature Mater. **10**, 273 (2011).

[6] X. Wang, T. Qian, P. Richard, P. Zhang, J. Dong, H. Wang, C. Dong, M. Fang, and H. Ding, *Strong Nodeless Pairing on Separate Electron Fermi Surface Sheets in* (T, K)$Fe_{1.78}Se_2$*) Probed by ARPES*, Europhys. Lett. **93**, 57001 (2011).

[7] D. Mou, Shanyu Liu, Xiaowen Jia, Junfeng He, Yingying Peng, Lin Zhao, Li Yu, Guodong Liu, Shaolong He, Xiaoli Dong *et al.*, *Distinct Fermi Surface Topology and Nodeless Superconducting Gap in a* $(Tl_{0.58}Rb_{0.42})Fe_{1.72}Se_2$ *Superconductor*, Phys. Rev. Lett. **106**, 107001 (2011).

[8] C. Chao and D. Jian-Hui, *Electronic Structure of* KFe_2Se_2 *from First-Principles Calculations*, Chin. Phys. Lett. **28**, 057402 (2011).

[9] L. Zhang and D. J. Singh, *Density Functional Study of the Overdoped Iron Chalcogenide* $TlFe_2Se_2$ *with* $ThCr_2Si_2$ *Structure*, Phys. Rev. B **79**, 094528 (2009).

[10] X.-W. Yan, X. F. Wang M. Gao, Z.-Y. Lu, and T. Xiang, *Electronic and Magnetic Structures of the Ternary Iron Selenides* AFe_2Se_2 *(*A = Cs, Rb, K, *or* Tl*)*, Phys. Rev. B **84**, 054502 (2011).

[11] K. Seo, B. A. Bernevig, and J. Hu, *Pairing Symmetry in a Two-Orbital Exchange Coupling Model of Oxypnictides*, Phys. Rev. Lett. **101**, 206404 (2008).

[12] C. Fang, H. Yao, W.-F. Tsai, J. Hu, and S. A. Kivelson, *Theory of Electron Nematic Order in LaFeAsO*, Phys. Rev. B **77**, 224509 (2008).

[13] F. Wang, H. Zhai, Y. Ran, A. Vishwanath, and D.-H. Lee, *Functional Renormalization-Group Study of the Pairing Symmetry and Pairing Mechanism of the FeAs-Based High-Temperature Superconductor*, Phys. Rev. Lett. **102**, 047005 (2009).

[14] I. I. Mazin, M. D. Johannes, L. Boeri, K. Koepernik, and D. J. Singh, *Problems with Reconciling Density Functional Theory Calculations with Experiment in Ferropnictides*, Phys. Rev. B **78**, 085104 (2008).

[15] A. V. Chubukov, D. V. Efremov, and I. Eremin, *Magnetism, Superconductivity, and Pairing Symmetry in Iron-Based Superconductors*, Phys. Rev. B **78**, 134512 (2008).

[16] T. A. Maier and D. J. Scalapino, *Theory of Neutron Scattering as a Probe of the Superconducting Gap in the Iron Pnictides*, Phys. Rev. B **78**, 020514 (2008).

[17] R. Thomale, C. Platt, J. Hu, C. Honerkamp, and B. A. Bernevig, *Functional Renormalization-Group Study of the Doping Dependence of Pairing Symmetry in the Iron Pnictide Superconductors*, Phys. Rev. B **80**, 180505(R) (2009).

[18] R. Thomale, C. Platt, W. Hanke, J. Hu, and B. A. Bernevig, Exotic d-Wave Superconducting State of Strongly Hole-Doped $K_xBa_{1-x}Fe_2As_2$, Phys. Rev. Lett. (to be published).

[19] Q. Si and E. Abrahams, *Strong Correlations and Magnetic Frustration in the High* T_c *Iron Pnictides*, Phys. Rev. Lett. **101**, 076401 (2008).

[20] M. Berciu, I. Elfimov, and G. A. Sawatzky, *Electronic Polarons and Bipolarons in Iron-based Superconductors: The Role of Anions*, Phys. Rev. B **79**, 214507 (2009).

[21] W.-Q. Chen, K.-Y. Yang, Y. Zhou, and F.-C. Zhang, *Strong Coupling Theory for Superconducting Iron Pnictides*, Phys. Rev. Lett. **102**, 047006 (2009).

[22] J. Dai, Q. Si, J.-X. Zhu, and E. Abrahams, *Iron Pnictides as a New Setting for Quantum Criticality*, Proc. Natl. Acad. Sci. U.S.A. **106**, 4118 (2009).

[23] S.-P. Kou, T. Li, and Z.-Y. Weng, *Coexistence of Itinerant Electrons and Local Moments in Iron-Based Superconductors*, Europhys. Lett. **88**, 17010 (2009).

[24] K. Haule, J. H. Shim, and G. Kotliar, *Correlated Electronic Structure of* $LaO_{1-x}F_xFeAs$, Phys. Rev. Lett. **100**, 226402 (2008).

[25] K. Haule and G. Kotliar, *Coherence–Incoherence Crossover in the Normal State of Iron Oxypnictides and Importance of Hund's Rule Coupling*, New J. of Phys. **11**, 025021 (2009).

[26] J. Wu and P. Phillips, *Experimental Detection of Sign-Reversal Pairing in Iron-Based Superconductors*, Phys. Rev. B **79**, 092502 (2009).

[27] M. Daghofer, A. Moreo, J. A. Riera, E. Arrigoni, D. J. Scalapino, and E. Dagotto, *Model for the Magnetic Order and Pairing Channels in Fe Pnictide Superconductors*, Phys. Rev. Lett. **101**, 237004 (2008).

[28] V. Mishra, G. Boyd, S. Graser, T. Maier, P. J. Hirschfeld, and D. J. Scalapino, *Lifting of Nodes by Disorder in*

Extended-s-State Superconductors: Application to Ferropnictides, Phys. Rev. B **79**, 094512 (2009).

[29] P. A. Lee and X.-G. Wen, *Spin-Triplet p-Wave Pairing in a Three-Orbital Model for Iron Pnictide Superconductors*, Phys. Rev. B **78**, 144517 (2008).

[30] V. Cvetkovic and Z. Tesanovic, *Multiband Magnetism and Superconductivity in Fe-Based Compounds*, Eur. Phys. Lett. **85**, 37002 (2009).

[31] K. Kuroki, S. Onari, R. Arita, H. Usui, Y. Tanaka, H. Kontani, and H. Aoki, *Unconventional Pairing Originating from the Disconnected Fermi Surfaces of Superconducting* $LaFeAsO_{1-x}F_x$, Phys. Rev. Lett. **101**, 087004 (2008).

[32] F. Wang, H. Zhai, and D.-H. Lee, *Antiferromagnetic Correlation and the Pairing Mechanism of the Cuprates and Iron Pnictides: A View from the Functional Renormalization Group Studies*, Europhys. Lett. **85**, 37005 (2009).

[33] S. Graser, T. A. Maier, P. J. Hirschfeld, and D. J. Scalapino, *Near-Degeneracy of Several Pairing Channels in Multiorbital Models for the Fe Pnictides*, New J. Phys. **11**, 025016 (2009).

[34] S. Graser, A. F. Kemper, T. A. Maier, H.-P. Cheng, P. J. Hirschfeld, and D. J. Scalapino, *Spin Fluctuations and Superconductivity in a Three-Dimensional Tight-Binding Model for* $BaFe_2As_2$, Phys. Rev. B **81**, 214503 (2010).

[35] A. Nicholson, W. Ge, X. Zhang, J. Riera, M. Daghofer, A. M. Oleś, G. B. Martins, A. Moreo, and E. Dagotto, *Competing Pairing Symmetries in a Generalized Two-Orbital Model for the Pnictide Superconductors* , Phys. Rev. Lett. **106**, 217002 (2011).

[36] J. Kang and Z. Tesanovic, *Theory of the Valley-Density Wave and Hidden Order in Iron Pnictides*, Phys. Rev. B **83**, 020505 (2011).

[37] S. Maiti and A. V. Chubukov, *Relation Between Nodes and* $2\Delta/T_c$ *on the Hole Fermi Surface in Iron-Based Superconductors*, Phys. Rev. B **83**, 220508 (2011).

[38] T. A. Maier, S. Graser, P. J. Hirschfeld, and D. J. Scalapino, *Inelastic Neutron and X-Ray Scattering as Probes of the Sign Structure of the Superconducting Gap in Iron Pnictides*, Phys. Rev. B **83**, 220505(R) (2011).

[39] R. Thomale, C. Platt, W. Hanke, and B. Andrei Bernevig, *Mechanism for Explaining Differences in the Order Parameters of FeAs-Based and FeP-Based Pnictide Superconductors*, Phys. Rev. Lett. **106**, 187003 (2011).

[40] V. Stanev, B. Alexandrov, P. Nikolic, and Z. Tesanovic, *Robust Accidental Nodes and Zeros and Critical Quasiparticle Scaling in Iron-Based Multiband Superconductors*, Phys. Rev. B **84**, 014505 (2011).

[41] W. Hanke, C. Platt, and R. Thomale, *Order-Parameter Anisotropies in the Pnictides—An Optimization Principle for Multi-Band Superconductivity*, Ann. Phys. (Berlin) **523**, 638 (2011).

[42] S. Maiti, M. M. Korshunov, T. A. Maier, P. J. Hirschfeld, and A. V. Chubukov, *Evolution of Superconductivity in Fe-Based Systems with Doping*, arXiv:1104.1814.

[43] Y.-Z. You, H. Yao, and D.-H. Lee, *The Spin Excitations of the Block-Antiferromagnetic State* $K_{0.8}Fe_{1.6}Se_2$, Phys. Rev. B **84**, 020406 (2011).

[44] T. A. Maier, S. Graser, P. J. Hirschfeld, and D. J. Scalapino, *d-Wave Pairing from Spin Fluctuations in the* $K_xFe_{2-y}Se_2$ *Superconductors*, Phys. Rev. B **83**, 100515(R) (2011).

[45] J.-X. Zhu, R. Yu, A. V. Balatsky, and Q. Si, *Local Electronic Structure around a Single Impurity as a Test of Pairing Symmetry in* $(K, Tl)Fe_xSe_2$ *Superconductors*, arXiv:1103.3509.

[46] M. M. Parish, J. Hu, and B. A. Bernevig, *Experimental Consequences of the s-Wave* $\cos(k_x)\cos(k_y)$ *Superconductivity in the Iron Pnictides*, Phys. Rev. B **78**, 144514 (2008).

[47] O. J. Lipscombe, G. F. Chen, C. Fang, T. G. Perring, D. L. Abernathy, A. D. Christianson, T. Egami, N. Wang, J. Hu, and P. Dai, *Spin Waves in the* $(\pi, 0)$ *Magnetically Ordered Iron Chalcogenide* $Fe_{1.05}Te$, Phys. Rev. Lett. **106**, 057004 (2011).

[48] F. Ma, W. Ji, J. Hu, Z.-Y. Lu, and T. Xiang, *First-Principles Calculations of the Electronic Structure of Tetragonal* $\alpha -$ FeTe *and* $\alpha -$ FeSe *Crystals: Evidence for a Bicollinear Antiferromagnetic Order*, Phys. Rev. Lett. **102**, 177003 (2009).

[49] C. Fang, B. Andrei Bernevig, and J. Hu, *Theory of Magnetic Order in* $Fe_{1+y}Te_{1-x}Se_x$, Europhys. Lett. **86**, 67005 (2009).

[50] Miaoyin Wang, Chen Fang, Dao-Xin Yao, GuoTai Tan, Leland W. Harriger, Yu Song, Tucker Netherton, Chenglin Zhang, Meng Wang, Matthew B. Stone, Wei Tian, Jiangping Hu, and Pengcheng Dai, *Spin Waves and Magnetic Exchange Interactions in Insulating* $Rb_{0.89}Fe_{1.58}Se_2$, arXiv:1105.4675.

[51] W. Bao, Q. Huang, G. F. Chen, M. A. Green, D. M. Wang, J. B. He, X. Q. Wang, and Y. Qiu, *A Novel Large Moment Antiferromagnetic Order in* $K_{0.8}F_{1.6}Se_2$ *Superconductor*, Chin. Phys. Lett. **28**, 086104 (2011).

[52] C. Fang, B. Xu, P. Dai, T. Xiang, and J. Hu, *Magnetic Frustration and Iron-Vacancy Ordering in Iron-Chalcogenide*, arXiv:1103.4599.

[53] Christian Platt, Ronny Thomale, Carsten Honerkamp, Shou-Cheng Zhang, and Werner Hanke, *Mechanism for a Pairing State with Time-Reversal Symmetry Breaking in Iron-Based Superconductors*, arXiv:1106.5964.

[54] J. Zhao, Dao-Xin Yao, Shiliang Li, Tao Hong, Y. Chen, S. Chang, W. Ratcliff, II, J. W. Lynn, H. A. Mook, G. F. Chen *et al.*, *Low Energy Spin Waves and Magnetic Interactions in* $SrFe_2As_2$, Phys. Rev. Lett. **101**, 167203 (2008).

[55] J. Zhao, D. T. Adroja, D.-X. Yao, R. Bewley, S. Li, X. F. Wang, G. Wu, X. H. Chen, J. Hu, and P. Dai, *Spin Waves and Magnetic Exchange Interactions in* $CaFe_2As_2$, Nature Phys. **5**, 555 (2009).

[56] M. Daghofer, A. Nicholson, A. Moreo, and E. Dagotto, *Three Orbital Model for the Iron-Based Superconductors*, Phys. Rev. B **81**, 014511 (2010).

[57] X. Lu, C. Fang, W. F. Tsai, Y. Jiang, and J. Hu, *s-Wave Superconductivity with Orbital Dependent Sign Change in the Checkerboard Models of Iron-Based Superconductors*, arXiv:1012.2566.

[58] D. Zanchi and H. J. Schulz, *Weakly Correlated Electrons on a Square Lattice: Renormalization-Group Theory*, Phys. Rev. B **61**, 13609 (2000).

[59] C. J. Halboth and W. Metzner, *Renormalization-Group Analysis of the Two-Dimensional Hubbard Model*, Phys. Rev. B **61**, 7364 (2000).

[60] C. Honerkamp, M. Salmhofer, N. Furukawa, and T. M. Rice, *Breakdown of the Landau-Fermi Liquid in Two Dimensions Due to Umklapp Scattering*, Phys. Rev. B **63**, 035109 (2001).

[61] C. Platt, C. Honerkamp, and W. Hanke, *Pairing in the Iron Arsenides: A Functional RG Treatment*, New J. Phys. **11**, 055058 (2009).

[62] S. Borisenko (unpublished).

[63] R. Yu, P. Goswami, Q. Si, P. Nikolic, and J. Zhu, *Pairing Strength and Symmetries of* $(\mathrm{K,Tl})\,\mathrm{Fe}_x\mathrm{Se}_2$ *in Comparison with Iron Pnictides*, arXiv:1103.3259.

[64] R. Yu, P. Goswami, and Q. Si, *Mott Transition in Modulated Lattices and Parent Insulator of* $(\mathrm{K,Tl})_y\mathrm{Fe}_x\mathrm{Se}_2$ *Superconductors*, Phys. Rev. Lett. **106**, 186401 (2011).

[65] Y. Zhou, D. Xu, F. Zhang, and W. Chen, *Theory for Superconductivity in* $(\mathrm{Tl,K})\mathrm{Fe}_x\mathrm{Se}_2$ *as a Doped Mott Insulator*, Europhys. Lett. **95**, 17003 (2011).

[66] F. Wang, F. Yang, M. Gao, Z. Y. Lu, T. Xiang, and D. H. Lee, *The Electron Pairing of* $\mathrm{K}_x\mathrm{Fe}_{2-y}\mathrm{Se}_2$, Europhys. Lett. **93**, 57003 (2011).